Sketch and Peel Focused Ion Beam Patterning of Black Phosphorus for Mid-Infrared Photonics

Huan Liu, Anders Barlow, Alexander Corletto, Christopher R. Hall, James Bullock, Shi Tang, Sivacarendran Balendhran, Seyed Saleh Mousavi Khaleghi, Sergey Rubanov, Trevor A. Smith, Yaping Dan, and Kenneth Crozier*

Black phosphorus (BP) is an important mid-infrared semiconductor, having a direct bandgap from monolayer (≈1.7 eV) to bulk (≈0.31 eV) thicknesses. The ability to nanopattern BP could enable new optoelectronic devices. However, existing nanopatterning techniques are either limited to thin flakes or produce BP with poor optical properties. Here, focused neon ion beam lithography is used to produce functional BP nanostructures. We demonstrate a "sketch and peel" method. The "sketch" step removes BP in a narrow line that outlines the desired structure. In the "peel" step, a hardened polymer droplet is used as a handle to pull off the surrounding flake. The "sketch and peel" method minimizes the damage to BP. We show that thermal treatment allows the small amount of damage that still occurs to be mitigated, as confirmed by Raman spectroscopy and mid-infrared photoluminescence. For the first time, this work demonstrates a method to nanopattern BP with very high resolution and to repair damage by producing high quality BP nanostructures. It thus could be an important enabling technology for future BP nanophotonic devices.

1. Introduction

The mid-wave infrared (MWIR, 3–5μm) spectral band is important for sensing because many molecular fingerprints are found within this region. Free-space optical communication also relies on this band due to its overlap with the window of atmospheric transparency. Interband cascade[1–3] and quantum cascade[4–6] lasers (ICLs, QCLs) are high performance MWIR sources. Typically, these are based on heterogeneous structures, e.g. III-V semiconductors such as InAs, GaSb, and AlSb. This necessitates the use of sophisticated and costly growth methods such as molecular beam epitaxy. Furthermore, while integration with complementary metal oxide semiconductor (CMOS) technologies would benefit many applications, it is non-trivial, requiring complex epitaxial growth or bonding techniques.

Black phosphorus (BP) is a direct bandgap semiconductor in all thicknesses, with a bandgap tunable from ≈1.7 eV (monolayer) to ≈0.31 eV (bulk).[7–10] The high photoluminescence quantum yield (PLQY) of its band-to-band emission in the bulk state (PLQY ≈1%)[10] makes it suitable as a platform for MWIR light generation.[11–14] Unlike the complex epitaxy growth techniques for III-V material in ICLs and QCLs, BP flakes can be easily exfoliated in a wide range of thickness (monolayer to μm)

H. Liu, K. Crozier
School of Physics
University of Melbourne
Parkville, VIC 3010, Australia
E-mail: kenneth.crozier@unimelb.edu.au

H. Liu, S. S. M. Khaleghi, Y. Dan
University of Michigan-Shanghai Jiao Tong University Joint Institute
Shanghai Jiao Tong University
Shanghai 200240, China

H. Liu, S. S. M. Khaleghi, K. Crozier
ARC Centre of Excellence for Transformative Meta-optical Systems (TMOS)
University of Melbourne
Parkville, VIC 3010, Australia

The ORCID identification number(s) for the author(s) of this article can be found under https://doi.org/10.1002/adom.202500460

A. Barlow
Materials Characterization and Fabrication Platform
University of Melbourne
Parkville, VIC 3010, Australia

A. Corletto, J. Bullock, S. Balendhran, S. S. M. Khaleghi, K. Crozier
Department of Electrical and Electronic Engineering
University of Melbourne
Parkville, VIC 3010, Australia

C. R. Hall, S. Tang, T. A. Smith
School of Chemistry
University of Melbourne
Parkville, VIC 3010, Australia

S. Rubanov
Bio21 Molecular Science & Biotechnology Institute
Faculty of Science
University of Melbourne
Parkville, VIC 3010, Australia

**ADVANCED
SCIENCE NEWS**

www.advancedsciencenews.com

**ADVANCED
OPTICAL
MATERIALS**

www.advopticalmat.de

and integrated into heterostructures. Furthermore, its self-terminating crystal structure and van der Waals interactions with other materials make BP compatible with CMOS platforms without lattice mismatch problems.[15–17] In addition, its in-plane anisotropy,[18] tunable optoelectronic properties,[19–23] and epsilon-near-zero property[24] present interesting opportunities for various optoelectronic devices.[25–30] The bio-medical potential of BP also attracts much attention recently due to its antimicrobial properties, which can enhance the wound healing process.[31–34]

Traditional lithography followed by reactive ion etching has been used to nanopattern 2D materials such as WSe_2, WS_2, hexagonal boron nitride (hBN), etc. without adverse effects due to their chemical stability. However, BP is known to be highly reactive with oxygen and water under light stimulation.[35] Thus, a multi-step fabrication process with constant exposure to the environment is unlikely to produce high-quality BP nanostructures. Furthermore, for many MWIR photonic integrated circuit components like waveguides and resonators, thick layers (100's nm or μm) are needed for optical mode confinement. Reactive ion etching would thus require long etching times, as the etching rate of BP is typically slow (e.g. O_2 plasma: 0.12 nm/s, Ar plasma: 0.5 nm/s [36]). A thick mask would thus be required to withstand the long etching time, which usually leads to poor lateral resolution. Scanning probe[37] and e-beam exposure[38] have been used to pattern BP monolayers and thin BP layers (10 to 40 nm thick), respectively. However, these techniques are hard to implement on thicker BP flakes (100's nm range).

Here, we use focused ion beam (FIB) with neon ions to nanopattern BP with very high resolution, i.e. down to ∼10 nm, for the first time to our knowledge. We demonstrate etching depths from tens of nm to more than one micron (1.1 μm), while retaining the optical properties of BP with minimal process damage. This is based on the "sketch and peel" method,[39–43] which has been previously used for evaporated gold films or gold flakes. In traditional FIB nanopatterning, the realization of an isolated structure involves removal of all surrounding material, which is slow and induces more material damage. We instead remove only the BP in a narrow cut that outlines the structure. This is referred to as the "sketch" step. We then attach a handle to the surrounding BP flake, i.e. outside the desired BP nanostructures. This comprises a droplet of polyvinyl acetate (PVA), which is dispensed onto the BP and allowed to dry. By pulling the handle away, we remove the surrounding BP flake and leave behind the desired isolated structure. This is referred to as the "peel" step. The "sketch and peel" method minimizes damage to BP and creates structure more efficiently because only the outline of the structure, rather than the entire surrounding material, is milled. We show that the FIB can create cuts as narrow as ∼10 nm. Using the "sketch and peel" technique, an isolated structure in the shape of an Australian koala is fabricated from a BP flake (∼700 nm thick). Tilted-angled helium ion microscopy (HIM) reveals that the structure has near-vertical sidewalls. We find that the BP near the cut (within a few microns) has modified properties. The Raman spectrum measured from this area has an elevated baseline in the region from ∼320 to ∼480 cm^{-1}. Nano-beam diffraction (NBD) in transmission electron microscopy (TEM) shows the amorphization of BP near the milling edge (∼ 500 nm wide). Electron energy loss spectra (EELS) measured in the same re-

gion show that there is more P than O, confirming that the modification corresponds to structural damage (i.e. amorphization) rather than chemical oxidization. Due to the structural damage, the mid-infrared photoluminescence (mid-IR PL) emission (peak wavelength ∼3.8 μm) is also decreased in strength. We demonstrate that a simple thermal treatment allows this to be restored, as revealed by the Raman spectrum having a flat baseline and sharp BP Raman modes, and by a near-doubling of the mid-IR PL emission. We believe that the "sketch and peel" method followed by thermal treatment is a useful contribution to a possible new field of BP nanophotonics.

2. Results and Discussion

Our gas-field ion source (GFIS) -based FIB system (Zeiss Orion) uses a well collimated neon ion beam emitted from one atom of the "trimer" (three atoms at the apex of a tungsten tip) under an acceleration voltage of 30 kV, schematically shown in **Figure 1a**. We first investigate the relationship between milling depth and dosage by milling a series of rectangles (size 1 μm × 5 μm) with dosages from 0.3 to 2.0 $nC/μm^2$ on a thick BP flake (∼1.1 μm), as shown in Figure 1b. We use atomic force microscopy (AFM) to map the topography of the milled rectangles. Figure 1c,d shows an AFM image of two rectangles (bottom: dosage 0.3 $nC/μm^2$, top: dosage 0.5 $nC/μm^2$) and their corresponding cross section profiles along the white dashed cutlines. AFM images of the other rectangles are provided in Supporting Information Figure S1 (Supporting Information). The milling depth (determined from AFM cross section profiles) versus dosage curve is shown as Figure 1e. The near linear relation confirms that the neon beam can mill BP to depths greater than 1 μm, which should suffice for most infrared optoelectronic devices. However, for high dosages, a racetrack-shaped blurred area is observed surrounding the milled rectangles, indicating damage to the BP. Redeposition and amorphization are commonly observed in the FIB patterning of materials like gold.[44,45] These add roughness and make the patterned shape depart from its target. For BP, there is another problematic side effect not seen in chemically inert materials such as gold. After being redeposited or amorphized, BP has dangling bonds, increasing the likelihood of interaction with oxygen or water vapor, the two key components involved in the degradation of BP.[35,46,47] This is consistent with the observation from laser scanning experiments on FIB-processed BP. The BP damage extending from the milling edge is accompanied by lower PLQY, caused by defects that are generated in the milling process (e.g. adding non-radiative recombination centers), which will be detailed in the following section.

As discussed earlier, material damage is minimized when utilizing the "sketch and peel" process because the area of the milled region is reduced as much as possible, i.e. only the edge of the desired nanostructures. Investigations into the resolution of this method consist of milling an array of patterns into a freshly exfoliated BP flake (∼100 nm thick). This comprises the logo of a research center with which some of the authors are affiliated ("TMOS", the ARC Centre of Excellence for Transformative Meta-Optical Systems), at three different sizes and linewidths (i.e. scaled versions at 100%, 50% and 25%). To avoid pre-exposure of the logo array region, neon beam alignment and focusing steps are done at the edge of the flake. The region into which the logo
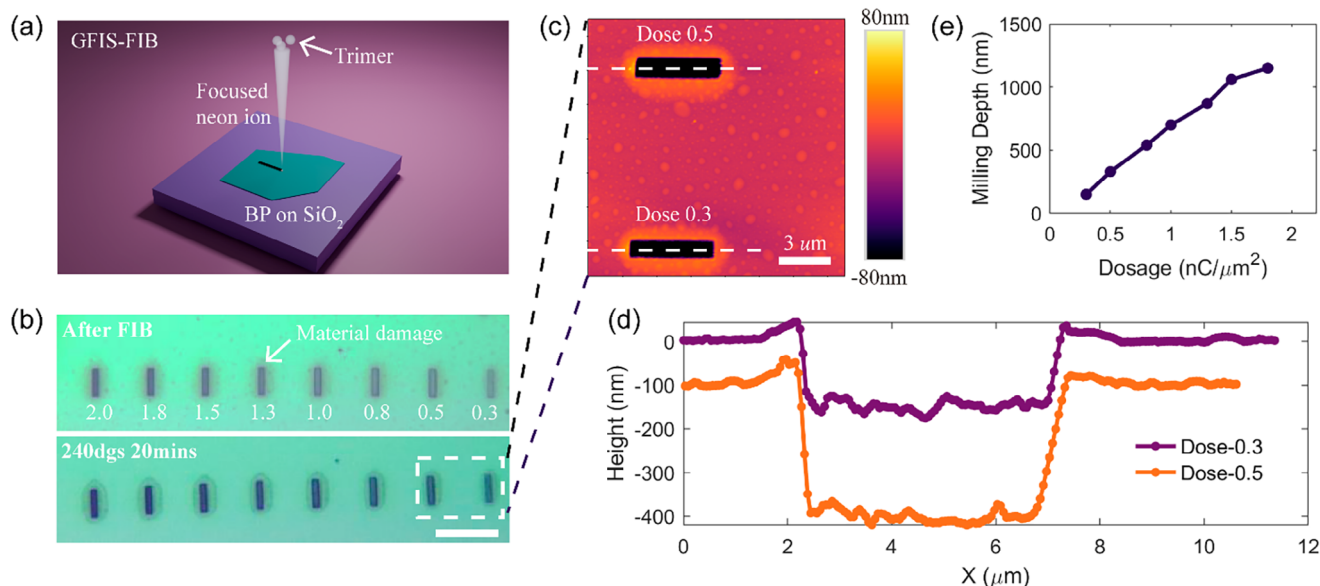
**ADVANCED
SCIENCE NEWS**

www.advancedsciencenews.com

**ADVANCED
OPTICAL
MATERIALS**

www.advopticalmat.de

Figure 1. Topology of FIB-patterned BP flake. a) Schematic view of gas-field ion source (GFIS)-based focused ion beam (FIB) patterning of BP flake. b) Optical microscope images of BP flake (~1.1 μm thick) on SiO$_2$ substrate with FIB-milled rectangles (1 μm × 5 μm size, dosage 0.3, 0.5, 0.8, 1.0, 1.3, 1.5, 1.8, 2.0 $nC/\mu m^2$ from right to left) before (top) and after (bottom) thermal treatment (240 °C for 20 minutes). Scale bar 10 µm. c) Atomic force microscopy (AFM) image of rectangles with dosages of 0.3 and 0.5 $nC/\mu m^2$ with cross section profiles (white dashed lines) plotted in (d). Cross section profile for 0.5 $nC/\mu m^2$ dose (orange line) is shifted downwards by 100 nm and leftwards by 500 nm for visualization purposes. e) Milling depth versus dosage for neon beam patterning of BP (30 kV acceleration voltage).

array is to be patterned (~20 µm away from the flake edge) is then moved to the center of field of view by the motorized sample stage. Neon beam patterning is then performed. Helium ion microscope (HIM) images of the nanopatterned region containing three "TMOS" logos are shown in **Figure 2a**. In the top logo, the vertical and horizontal sections of the letter "T" have widths of 200 nm (scale bar 1 µm). The middle and bottom logos are identical to the top logo, but scaled by 50% and 25%, respectively. Zoomed-in views of the 50% scaled and 25% scaled logos are shown as the upper and lower panels of Figure 2b, where the scale bars are 500 nm and 250 nm, respectively. The vertical and horizontal sections of the "T" in the smallest logo are 50 nm wide. The milled cuts are ~10 nm wide, much narrower than these sections (50 nm), which can be clearly seen from Figure 2c (scale bar 50 nm). It is also evident that neon-FIB achieves sharp corners. We study this by overlaying the edge-enhanced letter "T" outline with an arc of radius ~17 nm and two straight dashed lines in Figure 2d. It can be seen the two corners can be fitted. Thus, the radius of curvature of letter "T" is estimated to be ~17 nm, indicating the potential of Ne-FIB to achieve sharp features in the ~10 nm range. The edge-enhanced processing is done by applying a threshold function to the grayscale HIM image of the letter "T". The threshold function converts the grayscale image to a binary one, i.e. values larger or smaller than the threshold are set to be 0 (white in Figure 2d) or 1 (black in Figure 2d), respectively. This allows the location of the edge to be found. Our results show that a resolution of ~10 nm is achieved in the "sketch" step on BP. More HIM images of the repeat experiments ("TMOS" logo array) can be found in Figure S2 (Supporting Information).

We next discuss the "peel" step, where the goal is to remove the surrounding material. Here we use polyvinyl acetate (PVA) as the adhesive to stick to the surrounding material. A solution of PVA in water will form an adhesive thin film when it is dried. It has been used in "sketch and peel" on gold flakes to fabricate optical nanostructures.[39,40,43] Here, we apply it to BP. Using the "sketch" step described above, a structure with a koala shape is outlined into a BP flake. A PVA-based peel off process is then performed on a 2d material dry transfer system to remove the surrounding part. As illustrated in **Figure 3a**, the BP flake (containing the outlined koala-shaped structure) on a SiO$_2$/Si wafer with navigation markers is mounted on the transfer stage. Next, a droplet (~2 µL) of PVA/water solution is dispensed on a glass slide using a micropipette (I). The glass slide is then flipped over and fixed by a clamp mount, with the PVA droplet side towards the sample surface (II). The edge of the BP flake and the PVA droplet are brought into alignment by adjusting the mechanical translation stages holding the slide clamp and sample mount, while observing the process with an optical microscope. The sample stage is then lifted toward the PVA droplet until contact is made, followed by a further lifting to maximize the area of the flake covered by the droplet. Empirically, a contact ratio (defined as contact size/full flake size) greater than 0.5 tends to give a good success rate for the peeling step. During this process, we monitor the position of the edge of the PVA droplet (which we term the "flood line") in the optical microscope, to ensure that the PVA does not encroach onto the patterned area (III). After the PVA dries, which is indicated by it turning light yellow, the sample stage is slowly moved away from the glass slide. The part of the BP flake that surrounds the koala-shaped structure adheres to
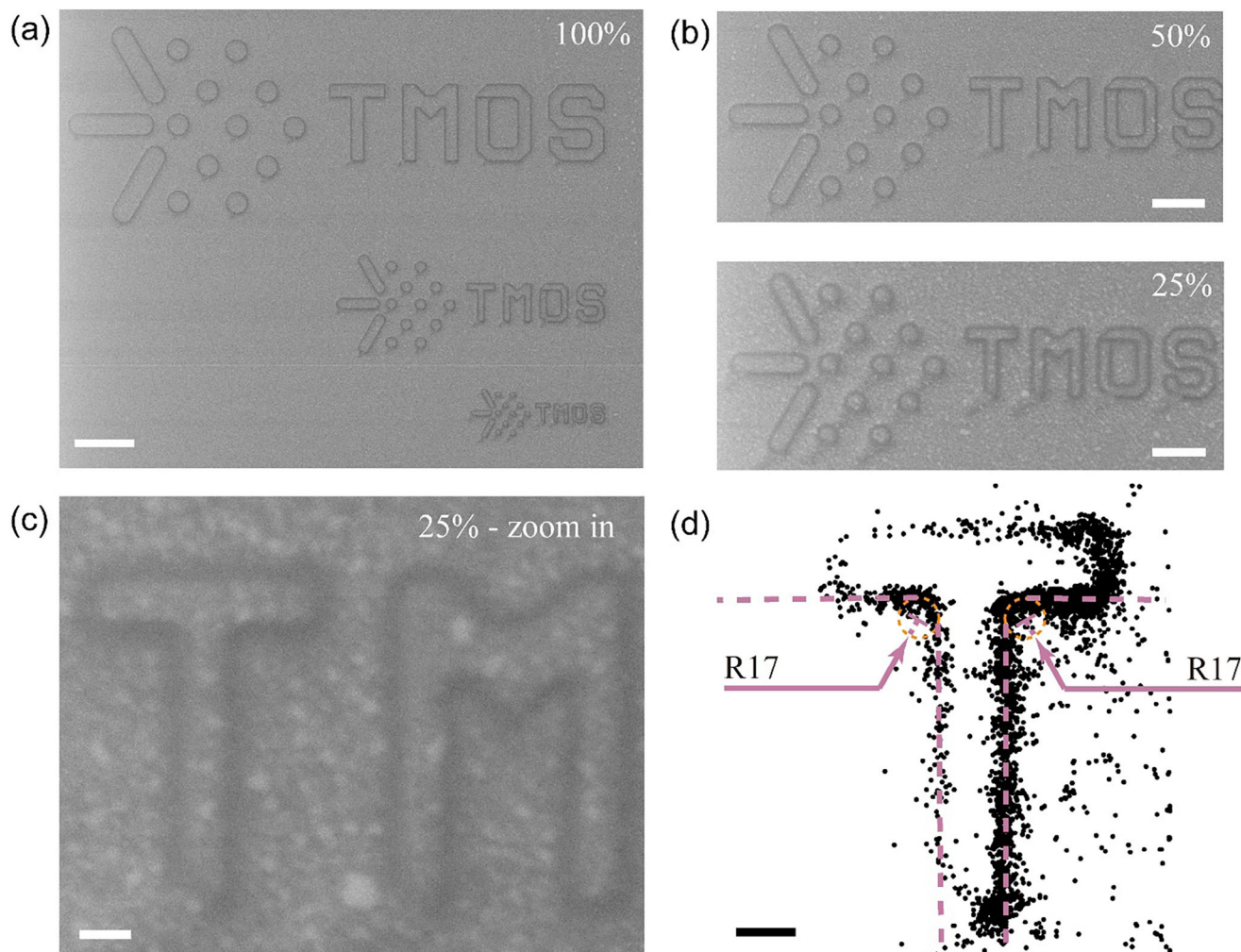
**ADVANCED
SCIENCE NEWS**

www.advancedsciencenews.com

**ADVANCED
OPTICAL
MATERIALS**

www.advopticalmat.de

Figure 2. Helium ion microscope images of Ne-FIB patterned TMOS logo array. a) Scale bar 1μm. b) Zoomed in view of the second (upper) and third (bottom) logo in (a). Scale bar 500 nm (upper), 250 nm (bottom). c) Zoomed in view of the bottom logo of (b). Scale bar 50 nm. d) Edge enhanced plot of letter "T" in (c) with curvature fitting process. Scale bar 50 nm.

the PVA film and thus peels off from the SiO_2/Si substrate (IV). This results in the isolated structure remaining on the SiO_2/Si wafer. This structure comprises the BP within the Ne beam outline, i. e. the koala-shaped pattern in Figure 3b. The bottom inset of Figure 3b shows the flake right after the "sketch" step. Considering that BP is less ductile than gold, which was used in previous reports of "sketch and peel", our use of the sample stage and glass slide provides better control over the sample and PVA droplet. Specifically, it allows slower and milder peeling of the PVA film with better reproducibility than just using tweezers by hand, as was done in previous work.[39,40,43] The AFM image of Figure 3c and the top inset of (b) show the 3D morphology of the koala-shaped structure (thickness ≈700 nm) and the zoomed-in view near the edge. An HIM image (tilt angle ≈85 °) of the koala-shaped structure is presented as Figure 3d. It is seen that the sidewalls are nearly vertical, which is a consequence of the low divergence of the Ne beam. However, some sign of material damage can be observed near the edge, namely that the BP within

~500 nm of the edge is different in thickness. This is discussed below.

Next, we study changes in the edge regions after neon milling by performing Raman spectroscopy on a BP sample with a "sketched" letter "T"-shaped structure (strip width 2 μm). The collected Raman signal is from a diffraction-limited region whose lateral extent is hundreds of nanometers or more. In **Figure 4a**, normalized Raman spectra are plotted when the laser spot is centered at the milling edge (x = −1 μm, magenta), near the milling edge (x = −2 μm, purple) of the letter "T", and at the center of the "T" strip (x = 0 μm, orange). The normalization of the Raman spectra is performed as follows. The raw spectra measured at the aforementioned three locations (at and near the milling edge, and at the center of the "T" strip) are divided by the peak value of the A_g^2 mode from the raw spectrum measured at ~3 μm from the milling edge, a location that is expected to be unaffected by the milling. In other words, if the normalized spectrum gives unity A_g^2 peak intensity, the BP at that

**ADVANCED
SCIENCE NEWS**

www.advancedsciencenews.com

**ADVANCED
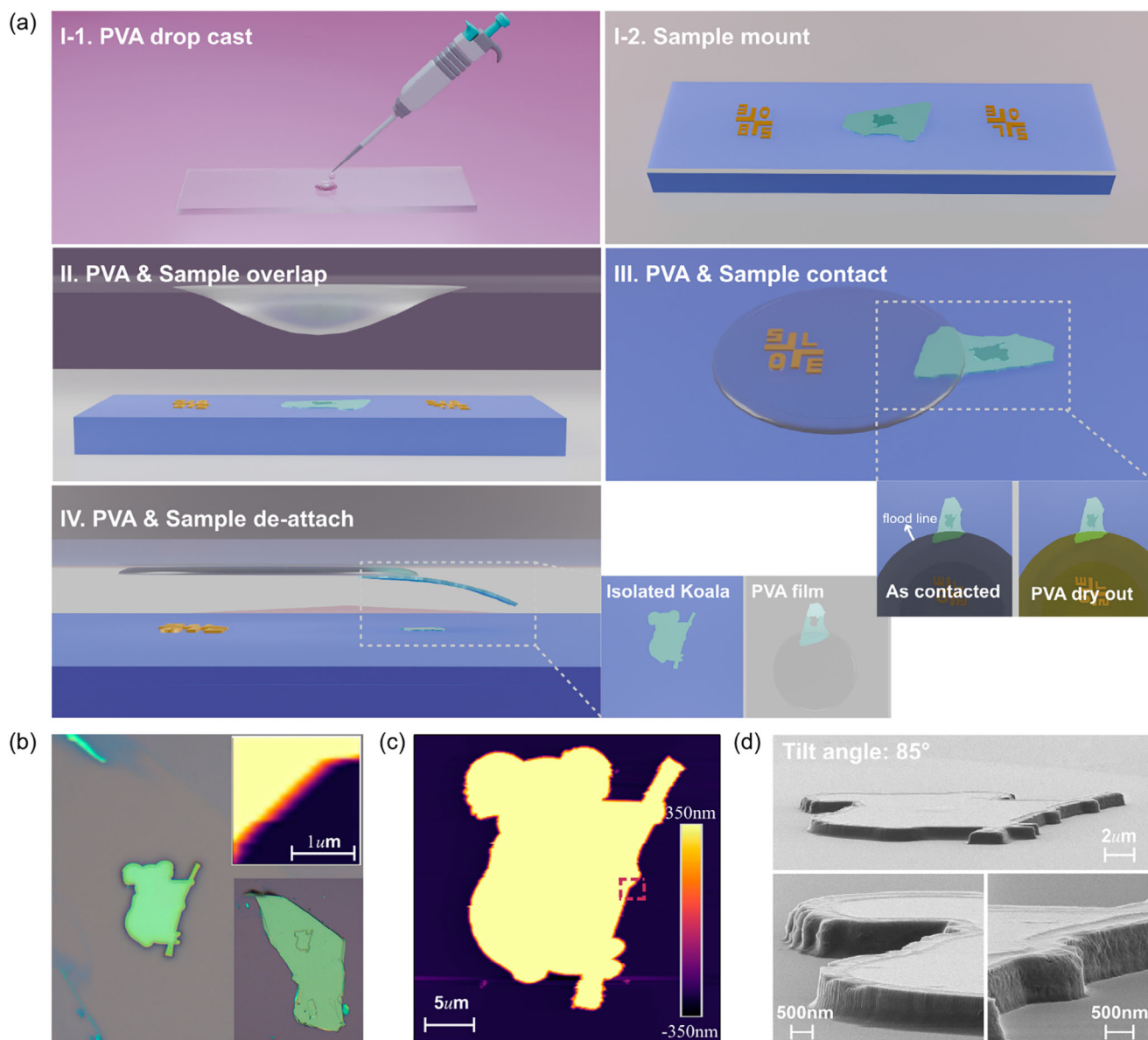OPTICAL
MATERIALS**

www.advopticalmat.de

Figure 3. Workflow for "peel" step and results for the koala-shaped BP structure. a) Peel-off workflow. I. PVA drop casting on glass slide. II. Flip over glass slide towards sample. III. PVA & sample contact. Zoom in illustrations show top view of PVA and BP after contact is made (left) and after PVA has dried out (right). IV. PVA & sample de-attach. Zoom in: "isolated koala" (left), peeled off PVA film (right). b) Optical microscope image of the koala-shaped BP structure resulting from "sketch and peel" process. Bottom inset: BP flake after "sketch" step. Top inset: zoomed-in AFM image near the edge marked by dashed red rectangle in (c). c) AFM image of koala-shaped structure after "sketch and peel" (d) Tilted-view (85°) helium ion microscope images of koala-shaped structure produced by "sketch-and-peel" after thermal treatment.

position has the same intensity as that of BP that should be fairly pristine. The sharp mode profiles (FWHM ≈4 cm^{-1} for three modes) and near-unity A_g^2 mode peak value near the milling edge (purple) and center of the "T" strip (orange) indicate that the quality of BP in these regions is similar to those of pristine BP.

On the other hand, at the milling edge (magenta), the mode profiles are broadened (FWHM, A_g^1: ~5 cm^{-1}, B_{2g}: ~7 cm^{-1}, A_g^2: ~4.5 cm^{-1}) and an elevated baseline emerges in the spectral range 320–480 cm^{-1}. This elevated baseline only appears in the

spectral range containing the BP modes, suggesting a connection with a distortion of the BP lattice. This elevated baseline has a shape similar to a previous report concerning the amorphous red phosphorus (ARP) system.[48] ARP usually has three fundamental modes (B, A$_1$, E) that correspond to different vibrations of those subunits. When under pressure, the subunits can be broken, can re-unite and can form larger chains, leading to an evolution of the Raman spectrum. At certain pressures, the three fundamental modes are broadened and merge to one wide peak that spans from 320 to 480 cm^{-1}.[48] The elevated baseline
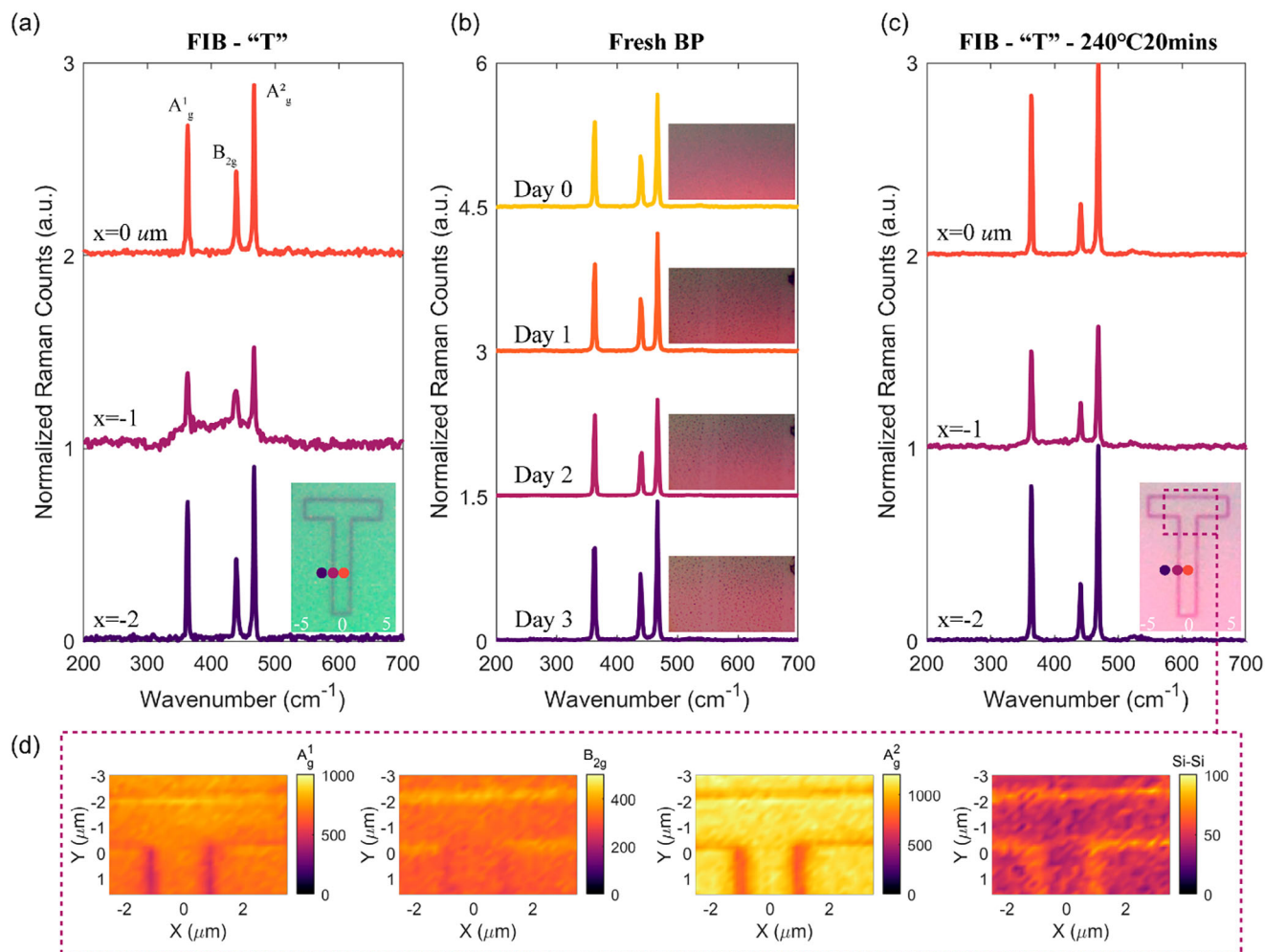
e00460 (5 of 11)

Figure 4. Confocal Raman characterization of fresh and FIB-sketched BP flakes (laser wavelength 532 nm, Renishaw inVia Qontor). Unless specified, the spectra are collected by a 100× objective with laser power is ~30 µW with an exposure time of 2 s. a) Normalized Raman spectra of FIB-sketched BP at an unaffected region (purple, bottom), milling edge (magenta, middle) and center of strip (orange, top). Spectra are normalized to peak intensity of A_g^2 BP mode, measured at ~3 µm from milling edge. b) Raman modes evolution over the course of four days, with sample stored in ambient dark conditions. c) Normalized Raman spectra of positions defined in (a) after thermal treatment (240 °C for 20 minutes). d) Spatial Raman peak intensity maps of BP's A_g^1, B_{2g}, A_g^2 modes and Si-Si bond within the purple dashed region indicated in (c)'s inset.

found in our FIB-sketched sample occupies a spectral region that matches that seen in ARP. This suggests that the baseline observed in our sample might have a similar origin to that seen in[48] for ARP, i.e. amorphization of the BP. This could be due to damage to the BP lattice by the Ne ions scattering. Another possible amorphization mechanism is material redeposition during FIB, which has been discussed before for other materials.[49,50] Naturally oxidized BP not patterned by FIB does not have these features, i.e. it has neither broadened Raman modes nor elevated baseline. We record Raman spectra from a fresh BP flake every day for four days, as shown in Figure 4b. Between measurements, the sample is stored in dark ambient conditions in the lab. The spectra are normalized to the Si-Si vibration mode (520.5 cm^{-1}) to correct for differences in laser power and detector responsivity that might occur between measurements. Optical microscope images in the inset of Figure 4b reveal the formation of bubbles on the surface starting from "Day 1", which is considered to be

a sign that the BP is oxidizing.[51–53] Since the penetration depth (probe depth) of the green laser (wavelength: 532 nm) is ~150 nm on BP, the Raman spectra measured is a combined contribution from oxidized BP layer and crystalline BP layer. If BP oxidation plays a role in the emergence of elevated baseline, then the resultant Raman spectra should be the mixture of the baseline and three BP modes. However, no mode broadening or elevated baseline appears during the course of the experiment (four days), which means oxidation doesn't account for this effect. Full size images of the flake from Day 0 to Day 3 are included in Figure S3 (Supporting Information).

Next, TEM and EELS are performed to explicitly reveal the structural and chemical properties of BP near the milling edge. A thin BP flake is transferred to a TEM carbon foil grid (1 µm diameter holes) and milled under the neon-FIB with a resultant 1 µm*5 µm rectangle, corresponding to the dark area in the inset of **Figure 5**a. The bright wavy shape surrounding the rectangle

**ADVANCED
SCIENCE NEWS**

www.advancedsciencenews.com

**ADVANCED
OPTICAL
MATERIALS**

www.advopticalmat.de

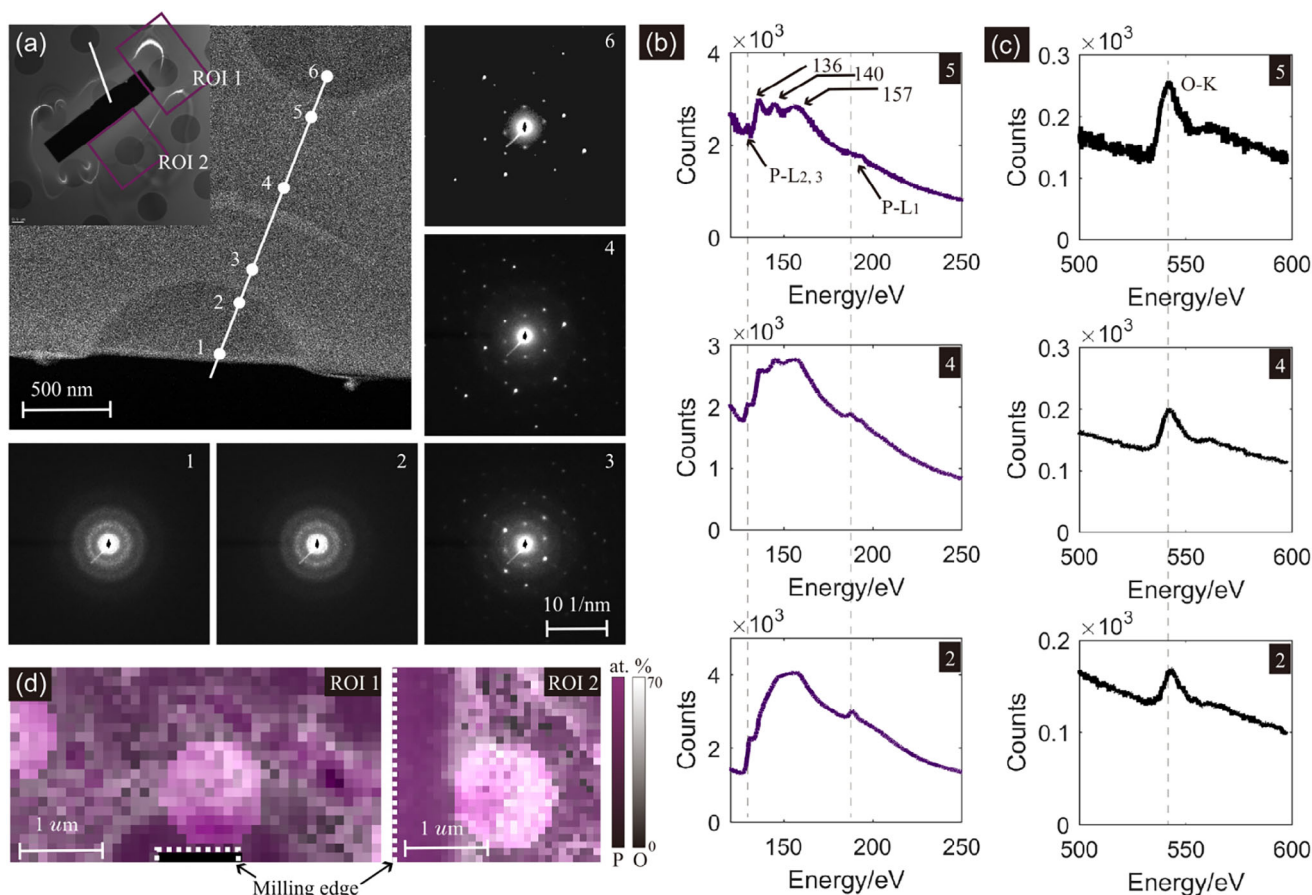**Figure 5.** TEM characterizations. a) Dark-field TEM image of the BP flake near the FIB-milled rectangular region (1μm × 5μm) and the corresponding NBD patterns (labelled 1-6) taken along the white guideline. Upper left inset: zoomed-out view of the milled area, highlighting the white cut line and two ROIs in (d). b) Deconvolved core-loss EELS spectra of P acquired at positions of 5, 4, 2 indicated in (a). Five types of transitions, previously reported in ref. [54] are labelled in the top panel, with characteristic transition energies at approximately 130 ($2p^{3/2} \rightarrow 3s$), 131 ($2p^{1/2} \rightarrow 3d$), 136 and 140 ($2p \rightarrow 3s/3d$ hybrid states), 157 ($2p \rightarrow 3d$), and 187 eV ($2s \rightarrow 3s/3d$), from left to right. The peaks at 130, 131 eV correspond to the well-known $P - L_{2,3}$ edges and the 187 eV feature corresponds to the $P - L_1$ edge. c) Deconvolved core-loss EELS spectra of O at the same position (5, 4, and 2), with the O-K edge indicated by a dashed line at ≈ 532 eV. d) Elemental composition maps showing the atomic percentages of P (purple) and O (white) in the two ROIs marked in (a). The white dashed lines indicate the outline of milled rectangle. The composition at each pixel is quantified based on the corresponding EELS core-loss spectra of P and O. Details of data analysis procedures can be found in Experimental section.

is the diffraction contour showing the strain-modified electron diffraction, which indicates the FIB-induced structural change to the material. NBD patterns along the white cut line are obtained, with representative ones labelled as 1, 2, 3, 4, 6 and shown in Figure 5a. For the NBD patterns measured close to the cut line (1, 2), only diffuse rings appear, indicating the full-amorphization of BP. Starting from spot 3 (~500 nm perpendicular distance from milling edge), some bright dots emerge, co-existing with the diffuse ring, implying a decreased level of amorphization. Going farther away to spot 4−6 (beyond 1 μm normal to milling edge), the diffuse ring region shrinks, with more and clearer diffraction spots, which shows that the crystallinity of BP is preserved well. This spatial extent of amorphization is consistent with our AFM and HIM observations. The deconvolved core-loss EELS spectra at positions 5, 4, 2 for P and O are plotted in Figure 5b and Figure 5c, respectively. At position 5, the main electronic transitions including P-$L_{2,3}$, P-L_1 and O-K lines are clearly resolved, which is consistent with previously reported

results.[54] Going closer to the milling region, i.e. position 4, the distinction between individual peaks is less pronounced, indicating the linewidth broadening after amorphization. In the fully amorphized region, e.g. position 2, only the P-$L_{2,3}$ and L_1 edges are clearly seen, with the rest of the peaks merging into a broad one. Interestingly, the peak intensity of the P (O) lines increases (decreases) upon entering the amorphized region, directly indicating that P (O) is more (less) prominent in the amorphized region compared to the unaffected area. This is more clearly visualized in the elemental composition color-mixing maps Figure 5d of two regions of interest (ROIs) marked in the inset of (a). The white dashed lines indicate the boundary of the milled rectangle (milling edge). The dark purple region near the milling edge (~500 nm wide) represents the aggregation of P and is consistent with the amorphized region. In this region, the O atomic percentage is mostly below 10%, while P remains around 35%. Beyond this region, O (white) becomes comparable to P (purple), or even exceeds it in some areas, indicating naturally oxidized

**ADVANCED
SCIENCE NEWS**

www.advancedsciencenews.com

**ADVANCED
OPTICAL
MATERIALS**

www.advopticalmat.de

yet crystalline BP. Therefore, we conclude that the FIB-induced damage is a localized structural amorphization confined to the milling edge vicinity. FIB-induced chemical oxidation is negligible, as evident from the low O atomic percentage in this region.

We next describe a thermal treatment method that enables the damage to be repaired. This involves annealing the BP flake (after FIB milling) on a hot plate (240 °C) in ambient conditions for 20 minutes. From Figure 4c, it is seen that this results in the elevated baseline disappearing and the Raman mode linewidths becoming narrower (FWHM, A_g^1: ~3 cm^{-1}, B_{2g}: ~4.5 cm^{-1}, A_g^2: ~3.5 cm^{-1}). Based on the findings of Refs,[48,55] we believe that two possible mechanisms are involved, either acting independently or coexisting. First, the amorphized BP reacts with oxygen and water, with the resulting products sublimating. In ref. [55], thermal annealing of BP was investigated and shown to be a useful way to thin down a BP flake. During the thermal annealing process, BP first becomes P_2O_3, P_2O_5 or H_3PO_4, in reaction with oxygen and water in the ambient. The P_2O_3 and H_3PO_4 then sublimate because the temperature exceeds their boiling points, leading to the continuous thinning of the BP. The P_2O_5, however, is quite stable, and can serve as a natural protective layer for BP. Ref.[55] reports that, at 240 °, the thinning rate is ~10 nm h^{-1} for crystalline BP. For our FIB-processed BP flake, we find that the regions near the milling edge are more sensitive to the ambient environment and to stimulation (e.g. laser scanning). We believe that it is reasonable to assume that the region near the milling edge will sublimate more rapidly during thermal treatment due to the large chance of dangling bonds experiencing exposure to the environment, meaning that the thickness change caused by thermal treatment will be greater for this region than the other parts of the BP flake. This could contribute to the thickness difference seen near the milling edge in Figure 3d. The thermal treatment method enables the removal of the amorphized BP in a gentle manner without causing damage to other parts of the BP flake. The other mechanism is that thermal treatment may also recrystallize part of the BP. However, further investigation is needed to verify this. To assess the quality of the BP after thermal treatment, we perform Raman mapping. The results are provided as Figure 4d. We map the peak intensities of the three Raman modes of BP (A_g^1, B_{2g}, A_g^2) and the Si-Si bond within the dashed rectangle region of Figure 4c. It can be seen from Figure 4d that the Raman mode intensities are quite uniform, which suggests that the BP is highly crystalline.

We next investigate the mid-infrared PL emission from BP and its enhancement by the thermal treatment. This is done in a home-built confocal mid-infrared photoluminescence scanning microscope, whose details are provided in Experimental Section. We present PL mapping results obtained after the FIB milling step as **Figure 6**a. It is seen that the PL signal (voltage reading from the amplified detector) within the patterned region (koala) is smaller (~7 μV) than that measured from the upper right corner (~14 μV). The latter is far (more than 20 μm away) from the FIB milling cut and should be unaffected by it. After the peel-off step, the resultant isolated BP pattern (koala) is clearly discernible in the PL map, though is blurry due to the pump laser spot size (diameter ≈5 μm). PL spectra measured before and after the thermal treatment are shown as Figure 6b. As described below, these spectra are corrected for detector response and are normalized. The spectra peak is at a wavelength of 3.8μm,

which is consistent with previous reports for bulk BP.[10,11,13] The spectra have pronounced dips at ~4.25 μm due to CO_2 absorption, a consequence of the fact that the system is not purged. Spectral correction is done by dividing the raw data by the responsivity of the InSb detector at each wavelength. The spectral response of the InSb detector is included as Figure S4 (Supporting Information). The spectra are then normalized to the peak intensity of the PL spectrum of the koala-shaped structure before the peel off step. From Figure 6b, it is seen that the PL intensity from the koala-shaped structure doubles after the thermal treatment. We also perform PL versus pump power measurements before and after thermal treatment, with the results shown as Figure 6c. The PL emission follows a linear trend with increasing pump power, indicating that the emitting system is still in the low-injection regime. As expected, the slope of linear fitting after thermal treatment is nearly double the value before (before: 1.84 μV/mW, after: 3.24 μV/mW). The enhancement can be attributed to the removal of non-radiative surface defects on the BP flake induced by the FIB milling. We also note that the PL from the koala-shaped structure after thermal treatment (~17 μV) is slightly stronger than that measured from the region well away (top right corner) from the milled area (~14 μV). This suggests that the thermal treatment allows the FIB-milled BP to recover its PL emission. Therefore, with proper thermal treatment, non-degraded PLQY from FIB-patterned BP is achieved.

3. Conclusion

In conclusion, a neon-FIB is used to nanopattern BP for the first time. We demonstrate milling depths exceeding 1 μm and cuts as narrow as ~10 nm with near-vertical sidewalls. We believe that material damage mainly consists of the amorphization of BP. Our use of the "sketch" step minimizes the material damage and beam time because we minimize the area of the region that needs to be milled by only milling the outline of the structure. The "sketch and peel" technique implemented is useful and efficient to fabricate isolated BP nanostructures. We show that BP damage near the milling edge can be mitigated by thermal treatment. This is shown by Raman spectroscopy and mid-IR PL measurements. The Raman spectra measured after thermal treatment have sharp Raman modes and no elevated baseline. The PL emission intensity is nearly doubled after thermal treatment. This work shows a method to nanopattern BP without causing deterioration of its properties, thereby presenting the opportunity for the realization of high-performance BP nanophotonic devices or circuits.[56–58]

4. Experimental Section

Sample Preparation: Thermal release tape is applied to the BP source crystal. This allows exfoliation of BP flakes onto the SiO$_2$ (280 nm)/Si substrate, which has pre-patterned Ti (10nm)/Au (45nm) markers for navigation. A flake with thickness ≈1.3 μm is used for the depth-dosage investigation. A flake with thickness ≈100 nm is selected for sculpting the "TMOS" logo array. A flake with thickness 700 nm is used for the "sketch and peel" nanopatterning of the koala-shaped structure. A flake with thickness ≈130 nm is selected for FIB sketch of the "T" shape and for performing Raman measurements before and after thermal treatment. A flake of thickness ≈300 nm is used for checking the evolution of the Raman spectra with

ADVANCED
SCIENCE NEWS

www.advancedsciencenews.com

ADVANCED
OPTICAL
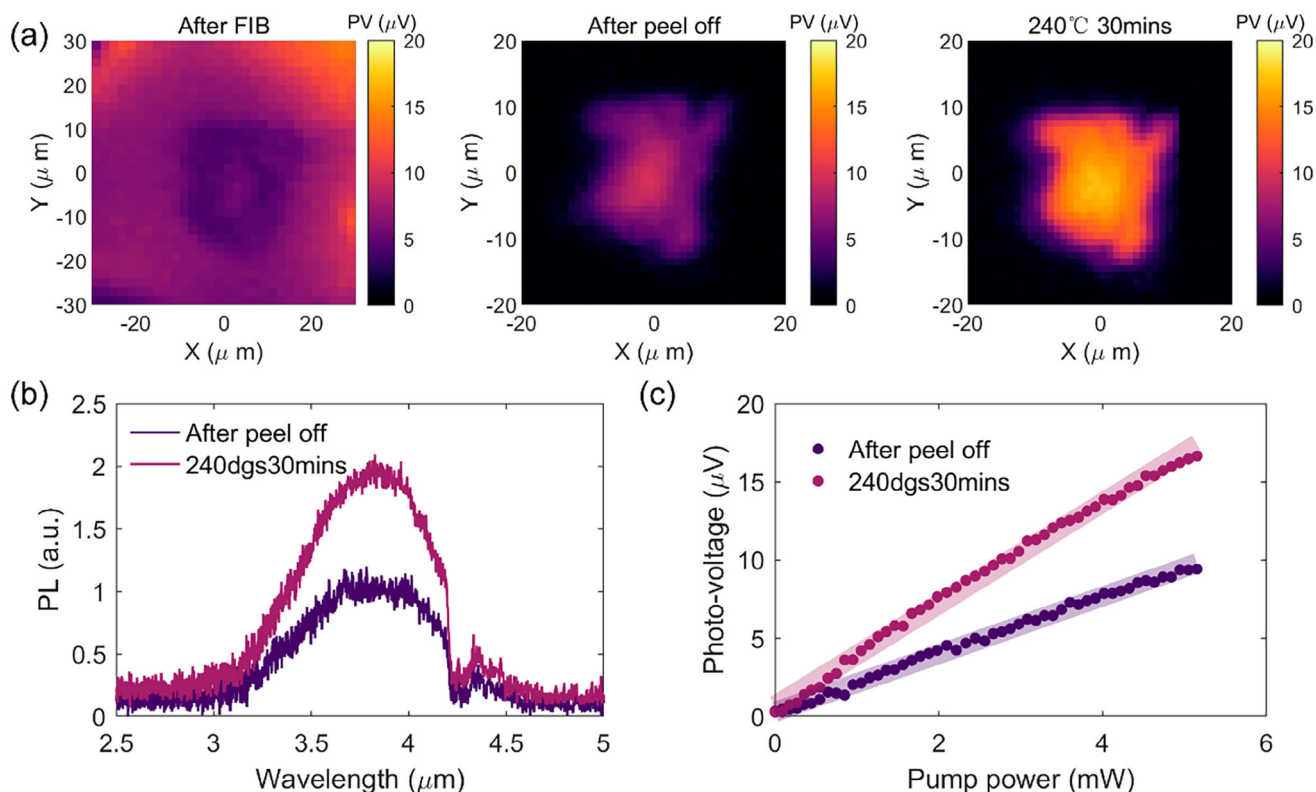**MATERIALS**

www.advopticalmat.de

Figure 6. Confocal MIR PL characterization of BP flake patterned into a koala-shaped structure. a) Mid-infrared photoluminescence mapping of the koala-shaped BP structure after FIB "sketch" step (left), after "peel" step (middle) and after thermal treatment (240 °C, 30 minutes) (right). Pump laser has a wavelength of 660 nm, a power of ~5 mW and a spot size of ~5 μm in diameter at the focal point. Long-pass filter (cut-on wavelength: 2400 nm) is used to filter out pump light. Color bar gives voltage from InSb detector unit. b) Photoluminescence spectra measured from koala-shaped structure before and after thermal treatment. Measurements are made at center of emission hotspots of the PL maps and performed at same pump power (~5 mW). c) Power-dependent photoluminescence from the koala-shaped BP structure before and after thermal treatment. Measurement position is the same as that used for panel (b). The straight semi-transparent lines are linear fits of the data.

natural oxidation. All flake thicknesses are determined using a profilometer (Dektak 150, Veeco).

Focused-Ion Beam Patterning: All patterning work is done in a dual-beam GFIS FIB nanofabrication system using a neon beam with a beam aperture size of 20 μm and beam current of ~4 pA. For sculpting the "TMOS" logo array, the field of view (FOV) is 10 μm. For the koala-shaped structure (which is thicker than the logo array), the FOV is 30 μm.

Confocal Mid-Infrared Photoluminescence Mapping/Spectrum System: A schematic diagram of the home-built confocal MIR PL system is shown in Figure S5 (Supporting Information). It consists of a microscope imaging section, an optical pumping section (laser with wavelength 660 nm, S1FC660, Thorlabs) and a PL emission section. During PL mapping, the FIB-patterned BP samples are mounted onto a two-channel motorized stage (MXY30, Thorlabs, min. step size 1 μm) to enable them to be scanned. During the measurements, a sinusoidally modulated (5 kHz) pump laser beam (wavelength: 660 nm) is incident on the BP flake. The as-modulated PL emission from BP is collected and collimated by a reflective objective (N.A. 0.3), then is focused by an off-axis parabolic mirror onto an InSb detector. A long-pass filter (cut-on wavelength 2400 nm) is used to block the scattered pump light. The InSb detector unit (KISDP-1-J1/DC, Kolmar) has an integrated transimpedance preamplifier, which produces an output voltage proportional to the photocurrent generated by the PL emission. This is input to a lock-in amplifier (Stanford Research Systems, SR865), with the reference signal comprising the modulation signal (5 kHz) provided to the pump laser. For spectrum acquisition, the signal is redirected by a flipped mirror into the FTIR (Frontier IR, Perkin Elmer) and

recorded with an InSb detector (INSB-1.0, InfraRed Associate). The signal is converted into a voltage by a transimpedance amplifier (INSB-1000, InfraRed Associate) and sent into the same lock-in amplifier. The FTIR is operated with an optical velocity of 0.1 cm/s and the time constant of the lock-in amplifier is set to 300 μs.

Polyvinyl Acetate (PVA) Solution Preparation: The PVA solution is prepared by dissolving PVA (molecular weight: 30 K, concentration: 100 mg mL^{-1}, Sigma Aldrich) in deionized water at 100 °C for 30 min, with vortex mixing at 600 rpm every 10 minutes.

Transmission Electron Microscopy and Electron Energy Loss Spectroscopy: The sample was examined using FEI Tecnai TF20 and TF30 transmission electron microscopes operated at 200 kV in TEM, STEM, and NBD modes. NBD data were collected with a parallel illumination (< 0.3 mrad) over a beam diameter of 5 nm across the cut line in Figure 5a in STEM mode with a step size of 45 nm. EELS measurements and spectrum imaging were conducted in STEM mode, with 1 nm probe beam diameter, convergence semi-angle of 2.2 mrad and collection semi-angle of 16 mrad at 200 kV (FEI Tecnai TF30) using Gatan GIF QuantumTM 965 energy filter with dual EELS capability. All TEM and EELS analyses were carried out using Gatan Digital Micrograph (DM) software. Raw EELS spectra are first aligned by their zero-loss peak to correct for spectral drift. Then, the Fourier-Log method is applied to remove the plural scattering, resulting in the deconvolved spectra shown as Figure 5b,c, which are used for further elemental quantification. Next, the core-loss regions, including the near-edge fine structures of P, O, C are fitted separately using reference standards in Gatan DM library, which incorporate empirical cross sections

**ADVANCED
SCIENCE NEWS**

www.advancedsciencenews.com

**ADVANCED
OPTICAL
MATERIALS**

www.advopticalmat.de

derived from known compounds and real measurement conditions (beam energy: 200 keV, convergence semi-angle: 2.2 mrad, collection semi-angle: 16 mrad). The integrated signals of the three elements are then scaled by their respective cross sections to yield the atomic density or atomic percentage at each probed position. Finally, the atomic percentage maps of the two ROIs are obtained as Figure 5d.

Supporting Information

Supporting Information is available from the Wiley Online Library or from the author.

Conflict of Interest

The authors declare no conflict of interest.

Data Availability Statement

The data that support the findings of this study are available from the corresponding author upon reasonable request.

[1] R. Q. Yang, *Superlatt. Microstruct.* **1995**, *17*, 77.
[2] M. Kim, C. L. Canedy, W. W. Bewley, C. S. Kim, J. R. Lindle, J. Abell, I. Vurgaftman, J. R. Meyer, *Appl. Phys. Lett.* **2008**, *92*, 191110.
[3] A. Spott, E. J. Stanton, A. Torres, M. L. Davenport, C. L. Canedy, I. Vurgaftman, M. Kim, C. S. Kim, C. D. Merritt, W. W. Bewley, J. R. Meyer, J. E. Bowers, *Optica* **2018**, *5*, 996.
[4] J. Faist, F. Capasso, D. L. Sivco, C. Sirtori, A. L. Hutchinson, A. Y. Cho, *Science* **1994**, *264*, 553.
[5] J. G. Coutard, M. Brun, M. Fournier, O. Lartigue, F. Fedeli, G. Maisons, J. M. Fedeli, S. Nicoletti, M. Carras, L. Duraffourg, *Sci. Rep.* **2020**, *10*, 6185.
[6] S. Jung, J. Kirch, J. H. Kim, L. J. Mawst, D. Botez, M. A. Belkin, *Appl. Phys. Lett.* **2017**, *111*, 211102.
[7] X. Wang, S. Lan, *Adv. Opt. Photon.* **2016**, *8*, 618.
[8] S. Huang, X. Ling, *Small* **2017**, *13*, 1700823.
[9] G. Zhang, S. Huang, F. Wang, H. Yan, *Laser Photonics Rev.* **2021**, *15*, 2000399.
[10] N. Higashitarumizu, S. Z. Uddin, D. Weinberg, N. S. Azar, I. K. M. Reaz Rahman, V. Wang, K. B. Crozier, E. Rabani, A. Javey, *Nature Nanotechnology* **2013**, *18*, 507.
[11] C. Chen, F. Chen, X. Chen, B. Deng, B. Eng, D. Jung, Q. Guo, S. Yuan, K. Watanabe, T. Taniguchi, M. L. Lee, F. Xia, *Nano Lett.* **2019**, *19*, 1488.
[12] Y. Huang, J. Ning, H. Chen, Y. Xu, X. Wang, X. Ge, C. Jiang, X. Zhang, J. Zhang, Y. Peng, Z. Huang, Y. Ning, K. Zhang, Z. Zhang, *ACS Photonics* **2019**, *6*, 1581.
[13] C. Chen, X. Lu, B. Deng, X. Chen, Q. Guo, C. Li, C. Ma, S. Yuan, E. Sung, K. Watanabe, T. Taniguchi, L. Yang, F. Xia, *Sci. Adv.* **2020**, *6*, aay6134.
[14] Y. Zhang, S. Wang, S. Chen, Q. Zhang, X. Wang, X. Zhu, X. Zhang, X. Xu, T. Yang, M. He, X. Yang, Z. Li, X. Chen, M. Wu, Y. Lu, R. Ma, W. Lu, A. Pan, *Adv. Mater.* **2020**, *32*, 201808319.
[15] C. Liu, J. Zheng, Y. Chen, T. Fryett, A. Majumdar, *Opt. Mater. Express, OME* **2019**, *9*, 384.
[16] T.-Y. Chang, Y. Chen, D.-I. Luo, J.-X. Li, P.-L. Chen, S. Lee, Z. Fang, W.-Q. Li, Y.-Y. Zhang, M. Li, A. Majumdar, C.-H. Liu, *Nano Lett.* **2020**, *20*, 6824.
[17] L. Filipovic, S. Selberherr, *Nanomaterials* **2022**, *12*, 12203651.
[18] V. Tran, R. Soklaski, Y. Liang, L. Yang, *Phys. Rev. B* **2014**, *89*, 235319.
[19] D. Çakır, H. Sahin, F. M. Peeters, *Phys. Rev. B* **2014**, *90*, 205421.
[20] J. Quereda, P. San-Jose, V. Parente, L. Vaquero-Garzon, A. J. Molina-Mendoza, N. Agraït, G. Rubio-Bollinger, F. Guinea, R. Roldán, A. Castellanos-Gomez, *Nano Lett.* **2016**, *16*, 2931.
[21] S. Huang, G. Zhang, F. Fan, C. Song, F. Wang, Q. Xing, C. Wang, H. Wu, H. Yan, *Nat. Commun.* **2019**, *10*, 2447.
[22] H. Kim, S. Z. Uddin, D-H. Lien, M. Yeh, N. S. Azar, S. Balendhran, T. Kim, N. Gupta, Y. Rho, C. P. Grigoropoulos, K. B. Crozier, A. Javey, *Nature* **2021**, *596*, 232.
[23] M. X. Low, S. A. Tawfik, S. P. Russo, S. Sriram, M. Bhaskaran, S. Walia, *ACS Appl. Nano Mater.* **2022**, *5*, 12189.
[24] S. Biswas, W. S. Whitney, M. Y. Grajower, K. Watanabe, T. Taniguchi, H. A. Bechtel, G. R. Rossman, H. A. Atwater, *Sci. Adv.* **2021**, *7*, abd4623.
[25] X. Chen, X. Lu, B. Deng, O. Sinai, Y. Shao, C. Li, S. Yuan, V. Tran, K. Watanabe, T. Taniguchi, D. Naveh, L. Yang, F. Xia, *Nat. Commun.* **2017**, *8*, 1672.
[26] B. Deng, V. Tran, Y. Xie, H. Jiang, C. Li, Q. Guo, X. Wang, H. Tian, S. J. Koester, H. Wang, J. J. Cha, Q. Xia, L. Yang, F. Xia, *Nat. Commun.* **2017**, *8*, 14474.
[27] S. Yuan, D. Naveh, K. Watanabe, T. Taniguchi, F. Xia, *Nat. Photon.* **2021**, *15*, 601.
[28] S. S. Jo, C. Wu, L. Zhu, L. Yang, M. Li, R. Jaramillo, *Adv. Photonics Res.* **2021**, *2*, 2100176.
[29] N. Matthaiakakis, S. Droulias, G. Kakarantzas, *Adv. Opt. Mater.* **2022**, *10*, 2102273.
[30] S. Lee, R. Peng, C. Wu, M. Li, *Nat. Commun.* **2022**, *13*, 1485.
[31] Y. Abate, D. Akinwande, S. Gamage, H. Wang, M. Snure, N. Poudel, S. B. Cronin, *Adv. Mater.* **2018**, *30*, 1704749.
[32] T. Guo, S. H. Zhuang, H. L. Qiu, Y. T. Guo, L. L. Wang, G. X. Jin, W. W. Lin, G. M. Huang, H. H. Yang, *Particle Particle Syst. Characterizat.* **2020**, *37*, 2000169.
[33] Z. L. Shaw, S. Cheeseman, L. Z. Y. Huang, R. Penman, T. Ahmed, S. J. Bryant, G. Bryant, A. J. Christofferson, R. Orrell-Trigg, C. Dekiwadia, V. K. Truong, J. P. Vongsvivut, S. Walia, A. Elbourne, *J. Mater. Chem. B* **2022**, *10*, 7527.
[34] E. P. Virgo, H. Haidari, Z. L. Shaw, L. Z. Y. Huang, T. L. Kennewell, L. Smith, T. Ahmed, S. J. Bryant, G. S. Howarth, S. Walia, A. J. Cowin, A. Elbourne, Z. Kopecki, *Adv. Therapeut.* **2023**, *6*, 2300235.
[35] S. Walia, Y. Sabri, T. Ahmed, M. R. Field, R. Ramanathan, A. Arash, S. K. Bhargava, S. Sriram, M. Bhaskaran, V. Bansal, S. Balendhran, *2D Mater.* **2016**, *4*, 015025.
[36] S. Kuriakose, T. Ahmed, S. Balendhran, G. E. Collis, V. Bansal, I. Aharonovich, S. Sriram, M. Bhaskaran, S. Walia, *Appl. Mater. Today* **2018**, *12*, 244.

**ADVANCED
SCIENCE NEWS**

www.advancedsciencenews.com

**ADVANCED
OPTICAL
MATERIALS**

www.advopticalmat.de

[37] X. Liu, K.-S. Chen, S. A. Wells, I. Balla, J. Zhu, J. D. Wood, M. C. Hersam, *Adv. Mater.* **2017**, *29*, 1604121.

[38] N. Clark, L. Nguyen, M. J. Hamer, F. Schedin, E. A. Lewis, E. Prestat, A. Garner, Y. Cao, M. Zhu, R. Kashtiban, J. Sloan, D. Kepaptsoglou, R. V. Gorbachev, S. J. Haigh, *Nano Lett.* **2018**, *18*, 5373.

[39] Y. Chen, Q. Xiang, Z. Li, Y. Wang, Y. Meng, H. Duan, *Nano Lett.* **2016**, *16*, 3253.

[40] Y. Chen, K. Bi, Q. Wang, M. Zheng, Q. Liu, Y. Han, J. Yang, S. Chang, G. Zhang, H. Duan, *ACS Nano* **2016**, *10*, 11228.

[41] M. Zheng, Y. Chen, Z. Liu, Y. Liu, Y. Wang, P. Liu, Q. Liu, K. Bi, Z. Shu, Y. Zhang, H. Duan, *Microsyst. Nanoeng.* **2019**, *5*, 54.

[42] M. Gittinger, K. Höflich, V. Smirnov, H. Kollmann, C. Lienau, M. Silies, *Nanophotonics* **2020**, *9*, 401.

[43] X. Wu, R. Ehehalt, G. Razinskas, T. Feichtner, J. Qin, B. Hecht, *Nat. Nanotechnol.* **2022**, *17*, 477.

[44] K. P. Müller, *Microelectron. Eng.* **1990**, *11*, 443.

[45] J. M. Cairney, P. R. Munroe, *Micron* **2003**, *34*, 97.

[46] T. Ahmed, S. Balendhran, M. N. Karim, E. L. H. Mayes, M. R. Field, R. Ramanathan, M. Singh, V. Bansal, S. Sriram, M. Bhaskaran, S. Walia, *npj 2D Mater. Appl.* **2017**, *1*, 18.

[47] S. Kuriakose, T. Ahmed, S. Balendhran, V. Bansal, S. Sriram, M. Bhaskaran, S. Walia, *2D Mater.* **2018**, *5*, 032001.

[48] H. Xiang, Y. Nie, H. Zheng, X. Sun, X. Sun, Y. Song, *Chem. Commun.* **2019**, *55*, 8094.

[49] J. Huang, M. Loeffler, U. Muehle, W. Moeller, J. J. L. Mulders, L. F. T. Kwakman, W. F. Van Dorp, E. Zschech, *Ultramicroscopy* **2018**, *184*, 52.

[50] Y. Huh, K. J. Hong, K. S. Shin, *Microsc. Microanal.* **2013**, *19*, 33.

[51] G. Abellán, S. Wild, V. Lloret, N. Scheuschner, R. Gillen, U. Mundloch, J. Maultzsch, M. Varela, F. Hauke, A. Hirsch, *J. Am. Chem. Soc.* **2017**, *139*, 10432.

[52] A. Ziletti, A. Carvalho, D. K. Campbell, D. F. Coker, A. H. Castro Neto, *Phys. Rev. Lett.* **2015**, *114*, 046801.

[53] J. Gómez-Pérez, B. Barna, I. Y. Tóth, Z. Kónya, Á. Kukovecz, *ACS Omega* **2018**, *3*, 12482.

[54] I. Benabdallah, Y. Auad, W. Sigle, P. A. van Aken, M. Kociak, M. Benaissa, *Mater. Sci. Eng., B* **2021**, *265*, 115002.

[55] S. Yang, A. Kim, J. Park, H. Kwon, P. T. Lanh, S. Hong, K. J. Kim, J. W. Kim, *Appl. Surf. Sci.* **2018**, *457*, 773.

[56] T. Ahmed, S. Kuriakose, E. L. H. Mayes, R. Ramanathan, V. Bansal, M. Bhaskaran, S. Sriram, S. Walia, *Small* **2019**, *15*, 1900966.

[57] J. Wu, H. Ma, P. Yin, Y. Ge, Y. Zhang, L. Li, H. Zhang, H. Lin, *Small Sci.* **2021**, *1*, 2000053.

[58] S. Kim, *Nanoscale Adv.* **2023**, *5*, 323.

e00460 (11 of 11)